

¹ Investigation of the causes of historical changes in the ² sub-surface salinity minimum of the South Atlantic

Marlos Goes,¹ Ilana Wainer,² and Natalia Signorelli²

Corresponding author: Marlos Goes, CIMAS/University of Miami and NOAA/AOML, Miami, USA. (marlos.goes@noaa.gov)

¹CIMAS/University of Miami and NOAA/AOML, Miami, USA.

²Institute of Oceanography, University of São Paulo, São Paulo, Brazil

3 **Abstract.**

4 In this study we investigate the sub-surface salinity changes on decadal
5 timescales across the Subtropical South Atlantic Ocean using two ocean re-
6 analysis products, the latest version of the Simple Ocean Data Assimilation
7 and the Estimating the Circulation and Climate of the Ocean, Phase II , as
8 well as with additional climate model experiments. Results show that there
9 is a recent significant salinity increase at intermediate levels. The main un-
10 derlying mechanism for this sub-surface salinity increase is the lateral ad-
11 vective (gyre) changes due to the Southern Annular mode variability, which
12 conditions an increased contribution from the Indian Ocean high salinity wa-
13 ters. The global warming signal has a secondary but complementary contri-
14 bution. Latitudinal differences at intermediate depth in response to large-
15 scale features are in part caused by local variation of westward propagation
16 features, and by compensating contributions of salinity and temperature to
17 density changes.

1. Introduction

18 Modulation and stability of the South Atlantic meridional overturning circulation are
19 dependent on salinity changes [*Weijer et al., 2002; Peeters et al., 2004*], and an improved
20 understanding of the mechanisms behind these salinity variations, especially the signature
21 of change below the ocean surface, is essential for better monitoring and prediction of
22 long-term climate change.

23 Long-term changes in ocean salinity are a function of large scale atmospheric forcing as
24 well as regional freshwater fluxes. In the South Atlantic Ocean significant ocean warming,
25 driving trends in freshwater fluxes, has been documented from observations and is the
26 subject of much research [*Gille, 2002; Curry et al., 2003; Boyer et al., 2005; Grodsky*
27 *et al., 2006; Boning et al., 2008; Schmidtko and Johnson, 2012; McCarthy et al., 2012*].
28 Ocean salinity changes are in general depth and latitudinally dependent [*Curry et al.,*
29 *2003*]. They are larger in the top 500 m of the ocean because of the direct effect of
30 atmospheric fluxes. In comparison to earlier data on record (1960–1970s), more recent
31 years (1990s) have shown salinity increases in the tropical-subtropical latitudes due to
32 warming and increased evaporation [*Boyer et al., 2005*], and salinity decreases in the
33 extratropical regions due to increased precipitation and runoff (including ice melting).

34 However, these long-term changes are subject to intense interannual and decadal vari-
35 ability [*Grodsky et al., 2006*], and more recent data show an actual decrease in surface
36 salinity in the tropical Atlantic due to increased precipitation and upwelling. This impacts
37 the mixed layer depth, and therefore the formation of subsurface water masses. Water
38 masses that are formed on the base of the mixed layer are in contact with the atmosphere

39 for a relative short period during their formation. They are eventually subducted into the
40 ocean interior following mostly an adiabatic pathway along neutral density surfaces. At
41 depth they are also modified by mixing which acts on much longer timescales. Below the
42 surface, the signature of salinity changes in the ocean is subject to higher uncertainty than
43 at the surface, since salinity is dynamically entangled with the temperature field, which
44 together determine the density [*Pierce et al.*, 2012]. Therefore, understanding salinity
45 changes in the South Atlantic at intermediate depths requires understanding the rela-
46 tive contribution of the associated processes [*Durack and Wijffels*, 2010], such as surface
47 atmospheric forcing, circulation changes, changes due to mixing along the water-mass
48 pathways, and vertical movements of isopycnals due to wind field effects. In the South
49 Atlantic, an important wind effect can be related to changes in the Southern Annular
50 Mode (SAM) through variations in sea level pressure (SLP), which in turn would impact
51 on the surface wind leading to a broad-scale surface warming associated with the pole-
52 ward migration of isopycnal outcrops [*Durack and Wijffels*, 2010; *Schmidtko and Johnson*,
53 2012].

54 Although frequent in situ salinity data are scarce in the South Atlantic before 2002,
55 several studies have used historical ship-based conductivity–temperature–depth (CTD)
56 along with more recent Argo floats data to investigate long-term changes in the Sub-
57 Antarctic Mode Water (SAMW) and in the Antarctic Intermediate Water (AAIW) salinity
58 minimum layer underneath. Their results indicate cooling and freshening of the SAMW,
59 and warming and salinification associated with the AAIW [*Bindoff and McDougall*, 1994;
60 *Boning et al.*, 2008; *McCarthy et al.*, 2011; *Schmidtko and Johnson*, 2012], in addition to
61 a statistically significant strong circumpolar AAIW isopycnals shoaling, accompanying a

62 decrease in density, and an equatorward spreading of the salinity anomalies at the sub-
63 surface [*Durack and Wijffels, 2010; Schmidtko and Johnson, 2012*]. A further decrease in
64 the AAIW density is also projected for the 21st century in climate models [*Goes et al.,*
65 2008].

66 Further analysis of Argo observations reveals the variability of the AAIW salinity in the
67 South Atlantic on interannual and intradecadal timescales. Westward propagating salinity
68 anomalies at 30°S show that Rossby wave mechanisms are important for the interpretation
69 of salinity changes associated with the hydrological cycle of the AAIW at these timescales
70 [*McCarthy et al., 2012*].

71 In this study we investigate changes in the sub-surface salinity minimum of the South
72 Atlantic and its relation to large-scale trends such as those related to global warming
73 via greenhouse gases and the Southern Annular Mode (SAM). For this we use a blend of
74 ocean reanalyses and process oriented climate model experiments. This paper is outlined
75 as follows: Section 2 describes the two ocean reanalyses used in this study; Section 3 shows
76 the results of the examination of the two reanalysis data, followed by the analysis of the
77 climate model experiments. The setup of the climate model experiments is presented in
78 an Appendix; Sections 4 and 5 contain a discussion of the results and the conclusion of
79 this study.

2. Data

80 The first part of this study utilizes temperature and salinity data from the Simple Ocean
81 Data Assimilation (SODA) version 2.2.6 [*Ray and Giese, 2012*], and from the Estimating
82 the Circulation and Climate of the Ocean, Phase II (ECCO2). They can be described as
83 follows:

2.1. SODA 2.2.6

84 SODA 2.2.6 uses the Parallel Ocean Program (POP) model [Smith et al., 1992] at
85 a $1/4^\circ$ horizontal resolution, which is publicly available at an interpolated $0.5^\circ \times 0.5^\circ$
86 horizontal resolution, and 40 vertical levels at monthly averages, spanning the period of
87 1871 to 2008. Vertical diffusion of momentum, heat, and salt are carried out using K-
88 profile parameterization (KPP) mixing with modifications to address issues such as diurnal
89 heating, while lateral subgrid-scale processes are modeled using biharmonic mixing.

90 Surface boundary conditions used are from eight ensemble members of the NOAA at-
91 mospheric Twentieth Century reanalysis 20Crv2 [Compo et al., 2011]. SODA 2.26 as-
92 simulates only sea surface temperature (SST) data using a sequential estimation data
93 assimilation method [Carton and Giese, 2008]. The SST data comes from the ICOADS
94 2.5 SST product (<http://icoads.noaa.gov>), which is based purely on in-situ observations
95 (e.g., XBT, CTD, bottle, Argo) and reached 2 million data report per year in 1960s. Heat
96 and salt fluxes in SODA are calculated from bulk formulae using 20CRv2 daily variables.
97 By not assimilating in-depth hydrography and only SST, the model is more dynamically
98 consistent over different decades than alternative versions. A complete overview of the
99 ocean-reanalysis process is detailed by Carton and Giese [2008].

2.2. ECCO2

100 The Estimating the Circulation and Climate of the Ocean, Phase II (ECCO2) project
101 [Menemenlis, 2008] An ECCO2 data synthesis is obtained by least-squares fit of a
102 global full-depth-ocean and sea-ice configuration of the Massachusetts Institute of Tech-
103 nology OGCM (Marshall et al. 1997) to the available satellite and in situ data. This
104 least-squares fit is carried out for a small number of control parameters using a Green's

105 function approach [Menemenlis, 2005]. The solution requires the computation of a
106 number of sensitivity experiments that are free, unconstrained calculations by a forward
107 model. The experiments are designed to adjust the model parameters, forcing, and initial
108 conditions. Then the model is run forward again using the adjusted parameters, free of
109 any constraints, as in any ordinary model simulation. The model employs a cube-sphere
110 grid projection with a mean horizontal grid spacing of 18 km and 50 vertical levels. Surface
111 forcings such as wind and precipitation are from the JRA25 reanalysis [Onogi, 2007].

3. Results

3.1. AAIW properties in SODA and ECCO2

112 As stated in the previous section, SODA 2.2.6 assimilates only SST data. This allows
113 the model to be more dynamically consistent over time, although larger differences may
114 exist with respect to actual hydrographic data. Salinity data in the South Atlantic are
115 historically sparse, mostly available in a more consistent way since the 2000s from Argo
116 floats measurements. ECCO2 uses a Green functions method, which also allows a smooth
117 salinity path over time, and allows a stronger hydrographic constraint with depth. We
118 estimate the differences in the representation of the AAIW in both reanalyses by com-
119 paring their salinity properties with an Argo climatology [Roemmich and Gilson, 2009],
120 which is available at a 1 degree horizontal resolution starting in 2004, for a similar pe-
121 riod. The Argo climatology exhibits a minimum salinity tongue in the central basin (at
122 25 °W; Figure 1c) extending from its formation region (between 45 and 60°S) across the
123 mixed layer to a maximum depth of 600–1200 m at 35–40°S. The salinity minimum follows
124 closely the depth of the isopycnal $\sigma_\theta = 27.2 \text{ Kg/m}^3$, which is approximately 1000 m deep
125 in this region. Previous studies have associated the depth of the salinity minimum with

126 the $\sigma_\theta = 27.2 \text{ Kg/m}^3$ isopycnal surface, and also with the neutral density surface $\gamma_n = 27.4$
127 Kg/m^3 [You, 2002]. North of 20°S , the $\sigma_\theta = 27.2 \text{ Kg/m}^3$ density surface levels out to
128 a depth of 700 m, and the salinity minimum flows underneath a salty surface region of
129 maximum evaporation minus precipitation (E-P).

130 SODA shows features analogous to the observations over a similar period (i.e., 2004–
131 2009; Figure 1a). In SODA, the isopycnals south of 40°S are much more inclined than
132 observations, and the maximum depth of the $\sigma_\theta = 27.2 \text{ Kg/m}^3$ is approximately 1200 m
133 deep, 200 m deeper than the observations. The salinity minimum in the South Atlantic
134 is also deeper in SODA than in the observations. This causes a maximum anomaly of
135 salinity on 40°S of up to 0.6 psu at 500 m depth (Figure 1d). At $\sim 7^\circ\text{S}$, SODA shows
136 a strong near-surface upwelling region, characterized by an uplifting of the isopycnals.
137 This feature is not evident in the ARGO climatology. ECCO2 shows a more consistent
138 structure than SODA, the minimum salinity is well constrained at approximately 800
139 m, and the differences of salinity with depth are therefore much reduced (< 0.2 psu) in
140 comparison to SODA (Figure 1e).

141 Next, we compare the regional features of the salinity minimum in the South Atlantic
142 between the reanalyses and Argo, doing so after interpolating all products to the Argo
143 resolution. The salinity minimum surface in the South Atlantic is shown in Figure 2.
144 SODA shows a stronger Subantarctic Front (STF; $\sim 45^\circ\text{S}$) than in observations (Figure
145 2a, c), which agrees with the larger isopycnal slopes in that region, as revealed in Figure
146 1a. For this reason the STF region shows the largest salinity differences (~ 0.3) between
147 SODA and Argo (Figure 2d). In the other regions salinity differences are smaller, and
148 can reach approximately 0.1 in magnitude. ECCO2 (Figure 2b) shows an improvement in

149 the STF region in comparison to SODA, and the biases are below 0.15 psu in the region.
150 North of 30°S, biases in ECCO2 and SODA show similar magnitudes. *Although there*
151 *are differences between the two reanalysis products and observations, their similarities,*
152 *and specially the dissimilarities with respect to the model assimilation schemes they are*
153 *based on, show that their temporal and spatial variability, once they agree between the*
154 *products, must be robust with respect to the variability of the AAIW in the region.*

3.2. Regional trends in the AAIW

155 In the South Atlantic, changes in the relationship of temperature and salinity along
156 isopycnals show latitudinal dependence. The time and latitude distribution of the South
157 Atlantic salinity at various density levels from the 1960s to 2000s is here inferred from
158 Temperature-Salinity (θ/S) diagrams for four latitudes (35°S, 30°S, 20°S, 10°S; Figure 3).

159 At 35°S (Figure 3a), SODA (solid lines) show strong salinity variability in the ther-
160 mocline waters. Salinity values are higher in the 2000s, although this increase is not
161 monotonic over time, instead alternating, with the 1970s and 1990s having lower salinity
162 values, and the 1960s, 1980s and 2000s having higher salinity values. Similar alternating
163 patterns are found along 30°S and 10°S (Figures 3b and 3d, respectively). At 10°S, which
164 is located in the tropical region of high E-P, salinity increases by 0.2 in the upper tropical
165 waters, which *is related to an increase in the hydrological cycle in the region [Curry et al.,*
166 *2003; Helm et al., 2010]*. At 20°S (Figure 3c), the 2000s SODA shows lower salinity values
167 at the thermocline, and higher values in the 1970s. The smallest differences in θ/S over
168 time are achieved at 20°S in the whole profile. The central and intermediate water levels
169 generally have opposing signs of changes at all latitudes. Central waters show a recent
170 cooling and freshening along isopycnals, as is apparent in the density layer between $\sigma =$

171 26.5 and 27.0 kg m⁻³, whereas intermediate waters generally show warming and increased
172 salinity between $\sigma = 27.2$ and 27.4 kg m⁻³ (highlighted in the insets of Figure 3). Central
173 water freshening has been suggested to be related to changes in subduction processes at
174 this density range [Durack and Wijffels, 2010]. ECCO2 (dashed lines) shows higher sur-
175 face salinities than SODA in the thermocline, specially at higher latitudes (Figures 3a,
176 b), and generally lower salinity values in intermediate levels. Salinity changes in ECCO2,
177 however, agree with SODA in that there is a salinity increase in the thermocline and
178 intermediate layers, and a decrease in the central water layers.

179 The spatial distribution of salinity minimum trends in SODA and ECCO are shown in
180 Figures (4a, b). For consistency, the trends are calculated since 1992 for the two products.
181 SODA and ECCO2 show an increase in the salinity minimum since 1992 almost everywhere
182 in the South Atlantic. Stronger changes are

183 To investigate how the trends in the dynamical parameters at the salinity minimum
184 position revealed in Figures (4a,b) are significant over time, we produce a time series
185 of the salinity, potential density (σ_θ) and temperature anomalies for SODA and ECCO2
186 relative to the SODA's average over its whole time series period at the depth of the salinity
187 minimum. We consider two locations in the central part of the basin, at 25°W/30°S
188 and 25°W/35°S (Figure 4). At both latitudes, SODA (black line) shows an increase in
189 salinity and temperature in the late 1980s/beginning of 1990s until the end of the series
190 (Figure 4c,g,d,h). This joint effect of warming and salinification produces a reduction in
191 density during this period (Figure 4e,f); a feature that agrees with climate projections
192 of the AAIW [Goes *et al.*, 2008]. The effect of the density decrease at the minimum
193 salinity depth is more prominent at 35°S than at 30°S. There is strong decadal variability

194 at both latitudes, although fluctuations appear in different periods: at 30°S, there is a
195 general freshening trend from the 1960s to the 1970s, and an increase in salinity after
196 1976 (Figure 4c). The rate of salinity increase from the mid-1970s to the mid-1990s is the
197 highest with about 0.01 per decade, while it levels out considerably in the late 1990s and
198 2000s. **At 35°S there is a significant positive salinity anomaly in the 1970s, followed by**
199 **an also significant negative salinity anomaly in the 1980s.** A linear trend of about 0.05
200 per decade is apparent after that. Trends observed in SODA after 2000 in all analyzed
201 parameters exceed 3 standard deviations (red dashed lines in Figure 4) calculated for the
202 whole time series period, showing that these trends are likely to be statistically significant.
203 Properties timeseries for ECCO2 (blue line) show much stronger variability than SODA,
204 which makes the detection of salinity changes since 1992 more difficult. However, property
205 changes in ECCO2 compares well with the ones from SODA for the same period.

206 The interannual-to-decadal salinity changes shown in Figure (4) are consistent with re-
207 cent findings that changes in the rate of global surface temperature increase have occurred
208 in previous decades, such as in the mid-1970s [*Levinson and Lawrimore, 2008; Trenberth*
209 *and Coauthors, 2007*], and that these changes can potentially produce signals in density
210 and salinity at depth [*Durack and Wijffels, 2010*].

3.3. Density changes in the subtropical Atlantic

211 According to *Bindoff and McDougall [1994]*, salinity changes at depth **have three main**
212 **causes:** i) freshening/salinification on isopycnals, ii) warming/cooling on isopycnals and
213 iii) heave, which is related to vertical displacements of isopycnals without changes in
214 salinity and temperature. Therefore, knowledge of these salinity changes requires under-
215 standing the causes of density changes at intermediate levels.

216 Timeseries in Figure 4 suggest that there is compensation between temperature and
217 salinity at the salinity minimum depth. An increase in salinity, which forces an increase
218 in density, is accompanied by an increase in temperature, and consequently a decrease in
219 density.

220 We investigate the causes of variability of density around the salinity minimum depth
221 (~ 1000 m) by estimating the thermopycnal and halopycnal changes at that depth. For
222 this we keep the salinity or temperature constant at their climatological means, and let the
223 other component vary over time. This way, we are able to estimate the main contribution
224 of density changes, which drive the large-scale meridional water displacement in the ocean.

225 The correlation between the thermopycnal and halopycnal terms provide information
226 of the compensation between these two terms (Figure 5). If the components are highly
227 negatively correlated, strong compensation is diagnosed. In opposition, weak or positive
228 correlation means that one of the terms is probably controlling the density changes. SODA
229 and ECCO2 show that there are dominant regions of compensation. Compensation occur
230 mostly in the middle of the subtropical gyre, where correlation between the thermal and
231 haline terms are often below -0.7 . In the regions that compensation happens, the individ-
232 ual components have weak correlation with density (not shown), therefore no contribution
233 is dominant. North of 30°S , the two components are positively correlated, and in this part
234 of the domain temperature is stronger driver of density changes.

235 This compensating behavior can explain the larger variability of salinity values on isopy-
236 cnals at 35°S than at 30°S , shown in Figure 4. Other studies have found similar compen-
237 sating patterns in the North Atlantic [*Lozier et al.*, 2010], where compensation on decadal
238 timescales is associated with water mass changes, rather than heave mechanisms. Since

239 ECCO2 reanalysis only spans for two decades, which would cast doubt on our ability to
240 meaningful interpret its changes as a part of a longer-term trend, we use SODA 2.2.6 in
241 the next two subsections to infer how salinity and gyre changes are inter-related in the
242 South Atlantic.

3.4. Subtropical Gyre variability

243 An AAIW layer, which encompasses the the salinity minimum surface depths (~ 800 –
244 1100 m), is constructed by defining two neutral density surfaces as the upper and lower
245 boundaries, the $\gamma_n = 27.1$ and $\gamma_n = 27.6$, respectively. Within this layer, there is a
246 signature of the inflow of salty Indian Ocean waters through the southeastern tip of the
247 Atlantic. The high salinity Indian Ocean waters at intermediate levels are formed in the
248 Red Sea [Talley, 2002]. After entering the South Atlantic, these waters lose their signature
249 through mixing along their trajectory westward. A **minimum on the salinity minimum**
250 **surface** is obvious at about 30°S (Figure 6a), crossing the basin from east to west following
251 the Benguela Current Extension [Schmid and Garzoli, 2009], which feeds into the Brazil
252 Current (BC) along the western boundary. BC waters encounter the Malvinas Current
253 waters between 35°S and 40°S, resulting in a westward inflow of low salinity waters along
254 the South Atlantic Current.

255 SODA shows decadal changes in salinity between the 1960 and 2000 (Figure 6b–e).
256 Compared to the 1960s, the 1970s and 1980s show a slight decrease in the minimum
257 salinity in most parts of the South Atlantic. A noticeable feature in the 1970s and later
258 on in the 1990s and 2000s is the southward shift of the Brazil-Malvinas confluence up to
259 about 3 degrees, in comparison to the 1960s. The 1980s, in opposition, shows a northward
260 migration of the confluence, which can explain some of the decadal variability shown in

261 **Figures 4**). The 1990s show reduced salinity in the center of the salinity minimum south
262 of 35°S, and a general increase of salinity in the rest of the basin. Of great importance
263 is the increased inflow of higher salinity waters from the Agulhas Current retroflection
264 region in the southeastern part of the basin, which increases the signature of these waters
265 toward the northwestern part of the basin. In the 2000s, this trend of increasing salinity
266 in the basin continues, and increased salinity values are found also on the western side
267 of the basin. This can have implications for the interhemispheric transport through the
268 North Brazil Undercurrent.

Advection mechanisms within the gyre have potential to drive a large part of the salinity increase displayed in SODA. This can be quantified by potential vorticity (PV) maps for the defined intermediate layer (Figure 7). The Ertel's PV is calculated as:

$$PV = \frac{f}{\rho_0} \frac{\Delta\gamma_n}{\Delta z} \quad (1)$$

269 where f is the Coriolis parameter, ρ_0 is the mean density of the ocean, and Δz is the
270 layer thickness. It is clear from the PV maps (**Figure 7**) that the PV has become more
271 negative inside the subtropical gyre at the AAIW layer, which characterizes a spin-up
272 of the anticyclonic gyre recently. Additionally, there has been an expansion of the gyre
273 southward, in agreement with observational results of the surface subtropical gyre [*Roem-*
274 *mich et al.*, 2007; *Goni et al.*, 2011], and poleward migration of the ACC [*Gille*, 2008].
275 This would preclude waters flowing from the Drake Passage and ACC from entering the
276 southern boundary of the South Atlantic, and would also reduce the mixing between the
277 Agulhas and SAC waters, making higher salinity waters prevail in the gyre.

3.5. Westward propagating Rossby Waves

278 As noted by *McCarthy et al.* [2012], salinity anomalies can be generated at intermediate
279 depths in the eastern side of the basin, and propagate westward with a second mode Rossby
280 wave speed. *McCarthy et al.* [2012] suggests that this can be an important mechanism to
281 explain the variability of the salinity minimum across the basin on interannual timescales.
282 In Figure 6, there is a clear extension of the subtropical gyre and increase in the Agulhas
283 leakage at intermediate depths. **????TALK ABOUT RELATIONSHIP BETWEEN WSC;
284 LATITUDE; STRENGTH)**

285 The Agulhas leakage is well correlated with the strength of the westerlies [*Durgadoo*
286 *et al.*, 2013] in the eastern part of the Atlantic basin. Similarly to *Durgadoo et al.* [2013],
287 we define an index for the strength of the westerlies in the eastern part of the basin as
288 the average zonal wind stress within 35°S–65°S and 0°W–20°E.

289 To investigate how salinity anomalies originated in the Agulhas leakage region and forced
290 by the westerly winds spread over the South Atlantic, we apply a lagged correlation of
291 the westerly wind stress index in the eastern side of the basin to the salinity minimum
292 surface. The time series are previously smoothed with a 9-month Boxcar window to filter
293 the seasonal variability. The maximum lagged correlations and their lags are shown in
294 Figure 8. The lag of the maximum correlation over space shows the propagation patterns
295 of the salinity anomalies. Small lag values, close to zero or even negative, are observed
296 in the eastern side of the basin. Negative lag values in the southeastern tip of the basin
297 show that the flow in the Agulhas leakage is driven in great part by the wind stress
298 anomalies east of Africa. Where the lag shows smaller values, the correlation of the
299 westerlies and the salinity anomalies is highest, above 0.6. Anomalies propagate along a

300 northwestern trajectory, following the ocean circulation at that depth (Figure 7). This is
301 also characteristic pattern of a Rossby wave signal, which phase speed decreases poleward.
302 A larger extension of anomalies propagation is revealed along 29°S. South of 30°S the lag
303 increases considerably up to 200 months, i.e., about 17 years.

304 To investigate whether Rossby wave propagation is a plausible dynamical mechanism
305 for the variability of the AAIW on interannual to decadal timescales, we produced time-
306 longitude plots (Hovmoller diagrams) at two latitudes, 30°S and 35°S (Figure 9). Hov-
307 moller diagrams allow us to determine zonal propagation patterns along a given latitude.
308 In these diagrams, propagating waves appear as diagonal bands across the basin, and
309 the slopes of these patterns are equal to the phase speed (c_p) of the waves. Here, wave
310 characteristics are assessed objectively using the Radon Transform (RT) applied to the
311 Hovmoller diagrams [*Challenor et al.*, 2001; *Polito and Liu*, 2003; *Barron et al.*, 2009].
312 This method rotates the coordinate system of the zonal-temporal diagrams in order to
313 find the patterns that best align with the rotated axis.

314 The Hovmoller diagrams are for salinity anomalies (calculated with respect to the an-
315 nual mean climatology) projected onto the $\gamma_n=27.4$ neutral surface. Zonal means are
316 subtracted from the anomalies field to filter decadal trends [*Barron et al.*, 2009], thus
317 highlighting the interannual timescales. West-to-east propagating anomalies spread along
318 30°S. The optimal propagation speed is $cp = 1.79 \pm 0.48$ cm s⁻¹, at which anomalies
319 travel across the basin in approximately 10 years. A similar result is obtained in the lag
320 correlation maps shown in Figure 8. These speeds strongly agree with those obtained by
321 *McCarthy et al.* [2012], who estimated a propagation speed of $cp = 1.7$ cm s⁻¹, which
322 is characteristic of a second baroclinic mode wave propagation. At 35°S, the situation

323 is different. Propagation speeds of $0.47 \pm 0.06 \text{ cm s}^{-1}$ are much slower than the one
324 predicted by the Rossby wave theory. In fact, the pattern of the variability in the eastern
325 part of the basin (east of 15°W) seems to be unrelated to the one further west. From the
326 lag correlation maps, we observe that the correlations decrease considerably from east to
327 west at this latitude, and therefore mixing and advective mechanisms must play a larger
328 role in the regional dynamics.

3.6. Wind x CO₂

329 In the previous sections we show that SODA 2.2.6 exhibits changes in the subsurface
330 salinity minimum and circulation patterns at intermediate layers. These changes include
331 decadal variability overlapping a background low frequency variability, which becomes
332 stronger after the 1970s. Other studies confirm that similar subsurface changes have
333 occurred since 1950 [e.g., *Levitus et al.*, 2000; *Gille*, 2002; *Levitus et al.*, 2005; *Domingues*
334 *et al.*, 2008; *Levitus et al.*, 2009; *Durack and Wijffels*, 2010; *Gille*, 2008; *Lyman et al.*,
335 2010].

336 In order to examine the possible causes of the salinity minimum variability, we perform
337 idealized experiments with an Earth System Model of Intermediate Complexity in which
338 two possible forcings, the wind stress curl changes in the Atlantic and the global warming
339 due to CO₂ are separated. In these experiments, we use the University of Victoria Earth
340 System Model of Intermediate Complexity (UVic 2.9) [*Weaver et al.*, 2001]. This model
341 has been widely used in climate simulations and model comparison studies. We separate
342 the influences of the wind stress on the advective mechanisms in the South Atlantic into
343 northern and southern hemispheric forcings, by defining the first hemispheric modes of
344 variability, which are related to the North Atlantic Oscillation (NAO) and SAM, to the

345 north and south respectively. A description of the model experiments can be found in
346 Appendix A.

347 **3.6.1. AAIW changes in the intermediate complexity model**

348 Similarly to Figure 4, we show the time series of salinity and temperature at the location
349 of the salinity minimum at 30°S and 25°W (Figure 10). For each index, four time series are
350 shown, which represent the index calculated for the experiments described in Appendix
351 A. The CONTROL simulation, without transient forcing (red curve), shows a salinity of
352 ~ 34.57 and temperature of ~ 4.39 °C from 1870 to 2009. Salinity changes, relative to
353 the CONTROL simulation, driven by wind changes in response to atmospheric pressure
354 changes due to the SAM (green curve in Figure 10a) are negative from 1870 to 1950 in
355 the model. Changes in the SAM phase after the 1960s drive positive salinity anomalies,
356 modulated by decadal variability. In 2008, the salinity is 0.015 above the pre-industrial
357 level. When a NAO-like forcing is considered in addition to the SAM forcing (blue curve
358 in Figure 10), additional changes are minor, and the trends due to wind variability in the
359 model resemble strongly the SAM-only experiment. Finally, when CO₂ forcing is added
360 on the top of SAM and NAO forcings (turquoise curve in Figure 10), there is an increased
361 positive trend in AAIW salinity after 1950 in comparison to the SAM-only experiment.
362 This trend driven by the CO₂ load in the atmosphere is strongly linear, and the 2008
363 salinity anomaly relative to the pre-industrial values is 0.025. Therefore, the CO₂ forcing
364 on AAIW salinity anomalies is responsible for 50% of the changes due to SAM in the
365 2000s. Although secondary in driving historical salinity anomalies in the AAIW, CO₂
366 forcing is the main contributor for the increase in temperature anomalies at the depth of
367 the salinity minimum (Figure 10b). While SAM-like forcing accounts for 0.1°C relative

368 to the CONTROL run, adding the CO₂ forcing increases the temperature anomalies to
369 0.3°C, a contribution of 2/3 of the recent warming of the AAIW, while SAM accounts for
370 just 1/3. NAO-like forcing is again a minor contribution to the AAIW variability in the
371 South Atlantic.

372 Salinity minimum changes in UVic are heterogeneous over the **spatial** domain (Figure
373 11). This feature agrees with those features manifested in SODA (Figure 6). Here we
374 separate the recent (2000s) effects of the considered external forcings on the salinity mini-
375 mum by subtracting hierarchically a simulation with that forcing from another simulation
376 without it.

377 Adding SAM as a forcing mechanism produces salinity anomalies with a dipole pattern
378 (Figure 11b), in which there is a salinity increase north of 35°S and mostly a decrease south
379 of 35°S. Anomalies generated by an NAO-like pattern (Figure 11c) are much reduced with
380 respect to the SAM or CO₂ forcings, and show mostly negative salinity anomalies within
381 the subtropical gyre. Forcing due to increased CO₂ concentration in the 2000s produce
382 a salinity increase in the subtropical South Atlantic, and negative anomalies along the
383 South Atlantic Current. The CO₂ response is similar but weaker than the response forced
384 by SAM, although south of 45°S the CO₂ response exhibits an increased salinity on the
385 northern edge of the ACC.

4. Discussion

386 Many physical processes can cause changes in the South Atlantic variability in partic-
387 ular, and in the Southern Hemisphere climate in general. These range from greenhouse
388 gases concentrations in the atmosphere (CO₂), to the major modes of coupled variabil-
389 ity. These atmospheric patterns can cause non-monotonic interdecadal fluctuations in the

390 θ/S relationships at depth, as revealed in previous studies [e.g., *Garabato et al.*, 2009].
391 SODA and the climate model experiments performed here show that the largest changes
392 in the salinity minimum are associated with changes in the gyre, and with trends in SAM,
393 which in turn will impact water mass formation processes through its relationship with
394 the associated surface winds. NAO variability largely affects Labrador Sea and Greenland
395 Sea water formation, and the water properties in the North Atlantic, especially the North
396 Atlantic Deep Water [*Arbic and Brechner Owens*, 2001]. According to our results, air-
397 sea climate modes in the North Atlantic do not seem to affect the spread of the salinity
398 minimum in the South Atlantic. The positive trend in SAM is associated with cooling at
399 high southern latitudes and strengthening of the latitudinal temperature gradient, leading
400 to stronger subtropical and westerly winds [*Hall and Visbeck*, 2002; *Silvestri and Vera*,
401 2003; *Lefebvre et al.*, 2004; *Sen Gupta and England*, 2006; *Gillett et al.*, 2006; *Toggweiler*
402 *et al.*, 2009; *Thompson et al.*, 2011]. The reader is referred to *Thompson et al.* [2011] for
403 an extensive review. In addition, *Durgadoo et al.* [2013] show from a hierarchy of mod-
404 els that an equatorward (poleward) shift in westerlies increases (decreases) the Agulhas
405 leakage. This occurs because of the redistribution of momentum input by the winds. It is
406 concluded that the reported present-day leakage increase could therefore reflect an unad-
407 justed oceanic response mainly to the strengthening westerlies over the last few decades.
408 *Bindoff and McDougall* [1994] analyze salinity and temperature changes in isopycnals as
409 pure heating, pure freshening and heave. More recent studies call attention to the lateral
410 advection of these properties along isopycnals, and therefore, circulation changes would
411 be a source of salinity changes on isopycnals [*Durack and Wijffels*, 2010]. Here we confirm
412 the role of lateral advection in reducing the low salinity waters from the Drake Passage due

413 to the Atlantic subtropical gyre expansion, as well as increasing leakage of salty Agulhas
414 waters at intermediate levels.

5. Conclusions

415 By investigating the decadal changes in the minimum salinity layer for the subtropical
416 South Atlantic we have established the relationship between density changes with large
417 scale climate trends. Significant trends are observed in SODA since the late 1990s in salin-
418 ity, temperature and density at intermediate levels. We found a latitudinal dependence
419 on the contribution of temperature and salinity to density changes that would ultimately
420 drive the meridional water displacement in the ocean. South of 30°S, and within the sub-
421 tropical gyre, there is strong compensation between salinity and temperature, which may
422 drive larger trends in those fields because of the dynamical influence of salinity. North of
423 30°S, temperature is by far the largest driver of density changes.

424 In SODA we determined two main dynamic factors for the salinity increase in the South
425 Atlantic salinity minimum region: i) the expansion and spinup of the subtropical gyre re-
426 duces the influx of the low salinity waters from the Pacific, which follow a path through
427 the Drake Passage into the South Atlantic; and ii) the strengthening of the westerlies
428 forces an increase in the Agulhas leakage, and, therefore, the input of high salinity waters
429 at intermediate depths into the South Atlantic. Different dynamic mechanisms are also
430 present at different latitudes which determine the spread of the high salinity waters from
431 the southeast boundary into the Atlantic. At 30°S, the anomalies generated by the west-
432 erlies in the southeastern Atlantic follow a path defined by the Benguela Current and the
433 Benguela Current Extension, in which changes in salinity at this latitude are highly driven
434 by ocean adjustment through a second mode Rossby wave mechanism. This result is in

435 agreement with previous studies [e.g., *McCarthy et al.*, 2012]. At 35°S, mixing is the main
436 mechanism to carry anomalies from the east, since propagation times are much larger than
437 what linear wave theory suggests, and the correlation with the eastern source of anomalies
438 is decreased. Previous studies have shown that bathymetric features, such as the Mid-
439 Atlantic Ridge can discontinue the propagation of Rossby waves westward [*Vianna and*
440 *Menezes*, 2013]. A more detailed analysis of the mixing properties and interaction with
441 abrupt bathymetry changes are beyond the scope of this paper.

442 The sensitivity studies with the UVic2.9 model indicate that the SAM is the predomi-
443 nant forcing of salinity changes in the sub-surface South Atlantic when compared to the
444 NAO and GHG forcing. GHG was shown to represent 50% of the changes due to SAM,
445 and therefore about 1/3 of the total magnitude of the salinity changes of the AAIW,
446 although GHG produces most of the temperature changes in the AAIW level.

Appendix A: The climate model of intermediate complexity

447 In the present work we use the latest version of the University of Victoria Earth System
448 Model (UVic 2.9). The ocean component of UVic 2.9 [*Weaver et al.*, 2001] is MOM2
449 [*Pacanowski*, 1995] with a 1.8° x 3.6° resolution in the horizontal and 19 depth levels.
450 Diapycnal diffusivity is parameterized as $K_v = K_{tidal} + K_{bg}$, which consists of the mixing
451 due to local dissipation of tidal energy (K_{tidal}) [*Laurent et al.*, 2002; *Simmons et al.*, 2004]
452 plus a background diffusivity $K_{bg} = 0.3 \text{ cm}^2 \text{ s}^{-1}$. The atmospheric component is a one-
453 layer atmospheric energy-moisture balance model, which does not apply flux correction
454 and is forced by prescribed winds from the NCEP/NCAR climatology. Also included in
455 the model are a thermodynamic sea ice component, a terrestrial vegetation (TRIFFID),
456 and an oceanic biogeochemistry based on the ecosystem model of [*Schmittner*, 2005]. The

457 model is spun up for 3000 years, and then four experiments are performed (Table 1).
458 First, the CONTROL experiment is a non-transient experiment forced with atmospheric
459 forcings from the 1800 levels. The second to fourth experiments use, in addition to the
460 NCEP/NCAR wind stress climatology, wind stress anomalies calculated from the first
461 empirical mode (EOF1) of sea level pressure (SLP) anomalies in the northern and southern
462 hemispheres (Figure 12). These modes are a good approximation of the North Atlantic
463 Oscillation (NAO), in which the positive phase is characterized by low SLP anomalies
464 over Iceland and high SLP anomalies over the Azores, and the Southern Annular Mode
465 (SAM), which is characterized by low SLP anomalies over Antarctica, respectively. More
466 specifically, the second experiment uses the SAM EOF forcing only, the third experiment
467 uses the NAO EOF forcing only, and the fourth experiment uses both the SAM and the
468 NAO forcings plus historical global CO₂ emissions, under which the atmospheric CO₂
469 concentration levels reach 384 ppmV in 2009. The hemispheric SLP modes are calculated
470 from the *Compo et al.* [2006] dataset and start in the year 1871. When the SLP anomalies
471 related to the hemispheric modes of variability are added to the model, the associated wind
472 stress anomalies are calculated using a frictional geostrophic approximation [*Weaver et al.*,
473 2001]. This wind stress is also converted to wind speed for the calculation of the latent
474 and sensible heat fluxes from the ocean [*Fanning and Weaver*, 1998]. All experiments are
475 run from 1800–2008, keeping the other atmospheric forcings (e.g., sulphate and volcanic
476 aerosols) at the 1800 level.

477 **Acknowledgments.** This work is supported in part by NOAA/AOML and NOAA's
478 Climate Program Office, and by grants from CAPES-ciencias-do-mar, 2013/02111-4 of the

References

- 481 Arbic, B. K., and W. Brechner Owens (2001), Climatic Warming of Atlantic Intermediate
482 Waters*, *J. Climate*, *14*, 4091–4108.
- 483 Barron, C. N., A. B. Kara, and G. A. Jacobs (2009), Objective estimates of westward
484 rossby wave and eddy propagation from sea surface height analyses, *J. Geophys. Res.*,
485 *114*, C03,013.
- 486 Bindoff, N. L., and T. J. McDougall (1994), Diagnosing climate change and ocean venti-
487 lation using hydrographic data, *J. Phys. Oceanogr*, *24*, 1137–1152.
- 488 Boning, C. W., A. Dispert, S. M. Visbeck, R. Rintoul, and F. U. Schwarzkopf (2008),
489 The response of the Antarctic Circumpolar Current to recent climate change, *Nature*
490 *Geosci.*, *1*, 864–869.
- 491 Boyer, T., S. Levitus, J. Antonov, R. Locarnini, and H. Garcia (2005), Linear trends in
492 salinity for the world ocean, 1955–1998, *Geophys. Res. Lett.*, *32*(1), 1–4.
- 493 Carton, J., and B. Giese (2008), A reanalysis of ocean climate using simple ocean data
494 assimilation (SODA), *Mon. Weath. Rev.*, *136*(8), 2999–3017.
- 495 Challenor, P. G., P. Cipollini, and D. Cromwell (2001), Use of the 3D radon transform
496 to examine the properties of oceanic Rossby waves, *J. Atmos. Oceanic Technol.*, *18*,
497 1558–1566.
- 498 Compo, G., J. Whitaker, and P. Sardeshmukh (2006), Feasibility of a 100-year reanalysis
499 using only surface pressure data, *Bull. Amer. Meteor. Soc.*, *87*, 175–190.

500 Compo, G., J. Whitaker, P. Sardeshmukh, N. Matsui, R. Allan, X. Yin, B. Gleason,
501 R. Vose, G. Rutledge, P. Bessemoulin, et al. (2011), The twentieth century reanalysis
502 project, *Quart. Jour. Royal Met. Soc.*, *137*(654), 1–28.

503 Curry, R., B. Dickson, I. Yashayaev, et al. (2003), A change in the freshwater balance of
504 the atlantic ocean over the past four decades, *Nature*, *426*(6968), 826–829.

505 Domingues, C. M., J. A. Church, N. J. White, P. J. Gleckler, S. E. Wijffels, P. M. Barker,
506 and J. R. Dunn (2008), Improved estimates of upper-ocean warming and multi-decadal
507 sea-level rise, *Nature*, *453*(7198), 1090–1093.

508 Durack, P., and S. Wijffels (2010), Fifty-year trends in global ocean salinities and their
509 relationship to broad-scale warming, *J. Climate*, *23*(16), 4342–4362.

510 Durgadoo, J. V., B. R. Loveday, C. J. C. Reason, P. Penven, and A. Biastoch (2013),
511 Agulhas leakage predominantly responds to the Southern Hemisphere westerlies, *J.*
512 *Phys. Oceanogr.*, *43*, 21132131.

513 Fanning, A. F., and A. J. Weaver (1998), Thermohaline variability: The effects of hori-
514 zontal resolution and diffusion, *J. Climate*, *11*(4), 709–715.

515 Garabato, A. C. N., L. Jullion, D. P. Stevens, K. J. Heywood, and B. A. King (2009),
516 Variability of subantarctic mode water and antarctic intermediate water in the drake
517 passage during the late-twentieth and early-twenty-first centuries, *J. Climate*, *22*(13),
518 3661–3688.

519 Gille, S. (2008), Decadal-scale temperature trends in the Southern Hemisphere ocean, *J.*
520 *Climate*, *21*, 4749–4765.

521 Gille, S. T. (2002), Warming of the southern ocean since the 1950s, *Science*, *295*, 1275–
522 1277.

523 Gillett, N., T. Kell, and P. Jones (2006), Regional climate impacts of the Southern Annular
524 Mode, *Geophys. Res. Lett.*, *33*(23).

525 Goes, M., I. Wainer, P. R. Gent, and F. O. Bryan (2008), Changes in subduction in the
526 South Atlantic Ocean during the 21st century in the CCSM3, *Geophys. Res. Lett.*, *35*,
527 6701–+.

528 Goni, G. J., F. Bringas, and P. N. DiNezio (2011), Observed low frequency variability of
529 the Brazil Current front, *J. Geophys. Res. – Oceans*, *116*(C10037).

530 Grodsky, S., J. Carton, and F. Bingham (2006), Low frequency variation of sea surface
531 salinity in the tropical Atlantic, *Geophys. Res. Lett.*, *33*(14), L14,604.

532 Hall, A., and M. Visbeck (2002), Synchronous variability in the Southern Hemisphere
533 atmosphere, sea ice, and ocean resulting from the annular mode*, *J. Climate*, *15*(21),
534 3043–3057.

535 Helm, K. P., N. L. Bindoff, and J. A. Church (2010), Changes in the global hydrological-
536 cycle inferred from ocean salinity, *Geophys. Res. Lett.*, *37*, L18701.

537 Laurent, L. S., H. Simmons, and S. Jayne (2002), Estimating tidally driven mixing in the
538 deep ocean, *Geophys. Res. Lett.*, *29*(23), 2106.

539 Lefebvre, W., H. Goosse, R. Timmermann, and T. Fichefet (2004), Influence of the South-
540 ern Annular Mode on the sea ice–ocean system, *J. Geophys. Res.: Oceans*, *109*(C9).

541 Levinson, D. H., and J. H. Lawrimore (2008), State of the climate in 2007, *Bull. Amer.*
542 *Meteor. Soc.*, *89*, S1–S179.

543 Levitus, S., J. Antonov, T. Boyer, and C. Stephens (2000), Warming of the world ocean,
544 *Science*, *287*, 2225–2229.

545 Levitus, S., J. I. Antonov, and T. P. Boyer (2005), Warming of the world ocean, 1955–2003,
546 *Geophys. Res. Lett.*, *32*, L02,604.

547 Levitus, S., J. Antonov, T. Boyer, R. Locarnini, H. Garcia, and A. Mishonov (2009),
548 Global ocean heat content 1955–2008 in light of recently revealed instrumentation prob-
549 lems, *Geophys. Res. Lett.*, *36*(7).

550 Lozier, M. S., V. Roussenov, M. S. C. Reed, and R. G. Williams (2010), Opposing decadal
551 changes for the North Atlantic meridional overturning circulation. *Nature Geosc.*, *3*,
552 728–734.

553 Lyman, J. M., S. A. Good, V. V. Gouretski, M. Ishii, G. C. Johnson, M. D. Palmer,
554 D. M. Smith, and J. K. Willis (2010), Robust warming of the global upper ocean,
555 *Nature*, *465*(7296), 334–337.

556 McCarthy, G., E. McDonagh, and B. King (2011), Decadal Variability of Thermocline and
557 Intermediate Waters at 24°S in the South Atlantic, *J. Phys. Oceanogr.*, *41*, 157–165.

558 McCarthy, G. D., B. A. King, P. Cipollini, E. L. McDonagh, J. R. Blundell, and A. Bi-
559 astoch (2012), On the sub-decadal variability of South Atlantic Antarctic Intermediate
560 Water, *Geophys. Res. Lett.*, *39*, L10,605.

561 D. Menemenlis, I. Fukumori, and T. Lee (2005), Using Green’s functions to calibrate an
562 ocean general circulation model. *Mon. Weather Rev.*, *133*, 1224–1240.

563 D. Menemenlis, J. Campin, P. Heimbach, C. Hill, T. Lee, A. Nguyen, M. Schodlok, and
564 H. Zhang (2008), ECCO2: High resolution global ocean and sea ice data synthesis.
565 *Mercator Ocean Quarterly Newsletter*, *31*, 13–21.

566 Onogi, K., J. Tsutsui, H. Koide, M. Sakamoto, S. Kobayashi, H. Hatsushika, T. Mat-
567 sumoto, N. Yamazaki, H. Kamahori, K. Takahashi, S. Kadokura, K. Wada, K. Kato, R.

568 Oyama, T. Ose, N. Mannoji, and R. Taira (2007), The JRA-25 Reanalysis, *J. Meteor.*
569 *Soc. Japan*, *85*, 369–432.

570 Pacanowski, R. (1995), MOM 2 documentation user’s guide and reference manual, GFDL
571 Ocean Group Technical Report No.3, *Fluid Dyn. Lab. NOAA, Princeton, NJ*.

572 Weijer, W., W. P. M. de Ruijter, A. Sterl, and S. S. Drijfhout (2002), Response of the
573 Atlantic overturning circulation to South Atlantic sources of buoyancy, *Global Planet.*
574 *Change*, *34*, 293–311.

575 Peeters, F. J. C., R. Acheson, G.-J. A. Brummer, W. P. M. de Ruijter, G. M. Ganssen,
576 R. R. Schneider, E. Ufkes, and D. Kroon (2004), Vigorous exchange between Indian
577 and Atlantic Ocean at the end of the last five glacial periods, *Nature*, *430*, 661–665.

578 Pierce, D. W., P. J. Gleckler, T. P. Barnett, B. D. Santer, and P. J. Durack (2012), The
579 fingerprint of human-induced changes in the oceans salinity and temperature fields,
580 *Geophys. Res. Lett.*, *39*, L21,704.

581 Polito, P. S., and W. T. Liu (2003), Global characterization of Rossby waves at several
582 spectral bands, *J. Geophys. Res.*, *108*(doi:10.1029/2000JC000607).

583 Ray, S., and B. S. Giese (2012), Historical changes in El Niño and La Niña characteristics
584 in an ocean reanalysis, *J. Geophys. Res.*, *117*, C11,007.

585 Roemmich, D., and J. Gilson (2009), The 2004-2008 mean and annual cycle of temper-
586 ature, salinity, and steric height in the global ocean from the Argo program, *Progr.*
587 *Oceanogr.*, *82*, 81–100.

588 Roemmich, D., J. Gilson, R. Davis, P. Sutton, S. Wijffels, and S. Riser (2007), Decadal
589 spinup of the South Pacific subtropical gyre, *J. Phys. Oceanogr.*, *37*, 162–173.

590 Schmid, C., and S. L. Garzoli (2009), New observations of the spreading and variability
591 of the Antarctic Intermediate Water in the Atlantic, *J. Marine Res.*, *67*(6), 815–843.

592 Schmidtko, S., and G. Johnson (2012), Multidecadal warming and shoaling of Antarctic
593 Intermediate Water*, *J. Climate*, *25*, 207–221.

594 Schmittner, A. (2005), Decline of the marine ecosystem caused by a reduction in the
595 Atlantic overturning circulation, *Nature*, *434*(7033), 628–633.

596 Sen Gupta, A., and M. H. England (2006), Coupled ocean-atmosphere-ice response to
597 variations in the Southern Annular Mode, *J. Climate*, *19*(18), 4457–4486.

598 Silvestri, G. E., and C. S. Vera (2003), Antarctic oscillation signal on precipitation anoma-
599 lies over southeastern South America, *Geophys. Res. Lett.*, *30*(21), 2115.

600 Simmons, H. L., S. R. Jayne, L. C. S. Laurent, and A. J. Weaver (2004), Tidally driven
601 mixing in a numerical model of the ocean general circulation, *Ocean Modell.*, *6*(3),
602 245–263.

603 Smith, R., J. Dukowicz, and R. Malone (1992), Parallel ocean general circulation model-
604 ing, *Physica D: Nonlinear Phenomena*, *60*(1), 38–61.

605 Talley, L. D. (2002), *Salinity patterns*, 11 pages pp., Encyclopedia of Global Environmental
606 Change, vol. 1, M. C. MacCracken and J. S. Perry, editors, John Wiley and Sons.

607 Thompson, D. W., S. Solomon, P. J. Kushner, M. H. England, K. M. Grise, and D. J.
608 Karoly (2011), Signatures of the Antarctic ozone hole in Southern Hemisphere surface
609 climate change, *Nature Geosc.*, *4*(11), 741–749.

610 Toggweiler, J., et al. (2009), Shifting westerlies, *Science*, *323*(5920), 1434–1435.

611 Trenberth, K. E., and Coauthors (2007), *Observations: Surface and atmospheric climate*
612 *change*, 235–336 pp., S. Solomon et al., Eds., Cambridge University Press.

613 Vianna, M. L., and V. V. Menezes (2013), Bidecadal sea level modes in the North and
614 South Atlantic Oceans, *Geophys. Res. Lett.*, *40*, 5926–5931.

615 Weaver, A. J., M. Eby, E. C. Wiebe, C. M. Bitz, P. B. Duffy, T. L. Ewen, A. F. Fanning,
616 M. M. Holland, A. MacFadyen, H. D. Matthews, et al. (2001), The UVic Earth system
617 climate model: Model description, climatology, and applications to past, present and
618 future climates, *Atmos.-Oc.*, *39*(4), 361–428.

619 You, Y. (2002), Quantitative estimate of Antarctic Intermediate Water contributions from
620 the Drake Passage and the southwest Indian Ocean to the South Atlantic, *J. Geophys.*
621 *Res.*, *107*, 3031.

Table 1. Summary of the climate model experiments.

Experiment	Wind Forcing	CO_2 Forcing
CONTROL	NCEP climatology	1800 level
SAM	NCEP clim plus SAM	1800 level
SAM + NAO	NCEP clim plus SAM plus NAO	1800 level
SAM + NAO + CO_2	NCEP clim plus SAM plus NAO	Transient to 384 ppmV in 2009

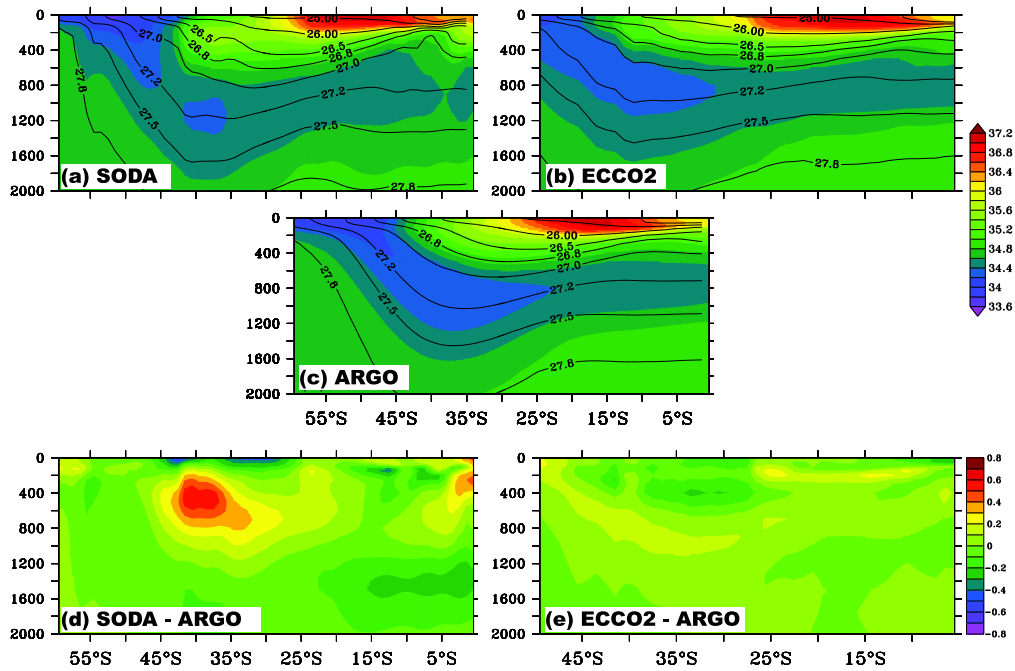


Figure 1. Meridional section of the climatological average (after 2004) of salinity at 25°W in the South Atlantic. Depth is in meters. Relevant potential density surfaces (σ_{θ} in Kg/m^3) are overlaid. Panel a) is for SODA, b) for ECCO2, c) for Argo climatology [Roemmich and Gilson, 2009], d) SODA - Argo and e) ECCO2 - Argo.

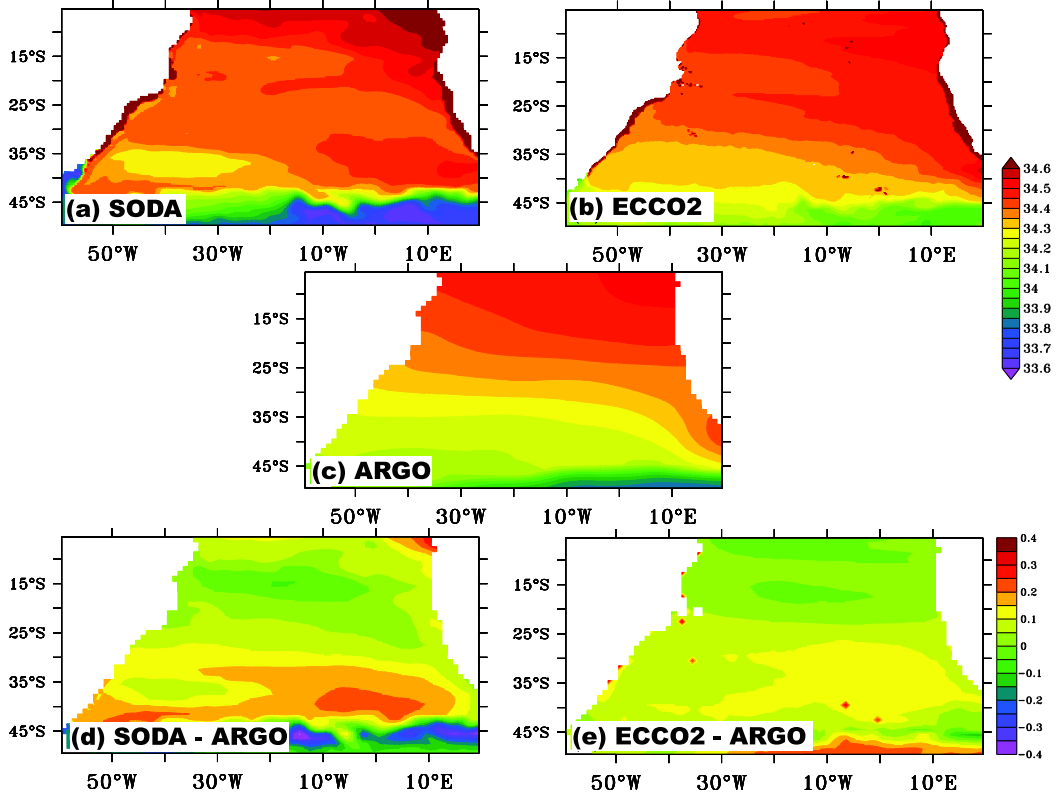


Figure 2. Maps of the climatological average (after 2004) of the salinity minimum surface in the South Atlantic. Panel a) is for SODA, b) for ECCO2, c) for Argo climatology [Roemmich and Gilson, 2009], d) SODA - Argo and e) ECCO2 - Argo.

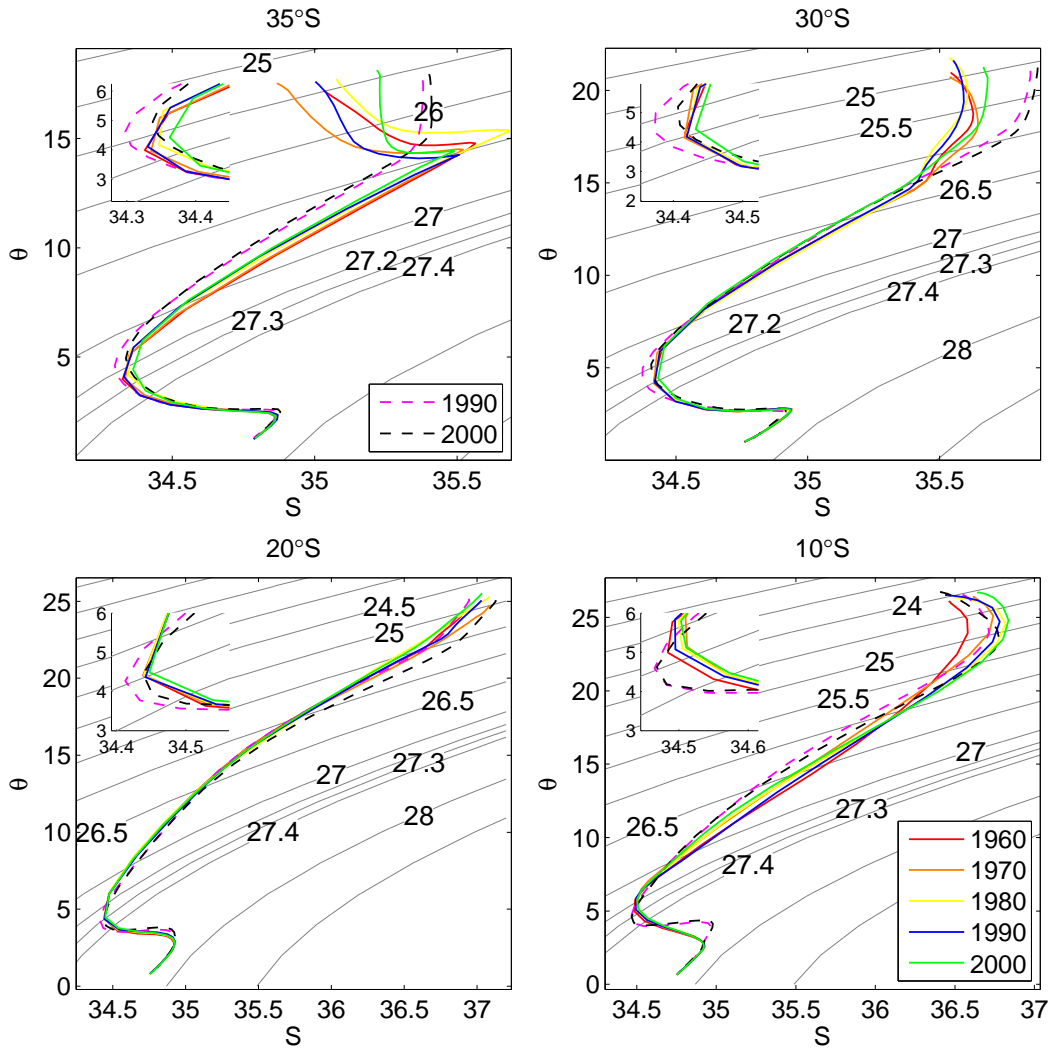


Figure 3. Θ/S diagram for the South Atlantic Ocean at 25°W for a) 35°S , b) 30°S , c) 20°S and d) 10°S . Solid colored lines represent SODA's decadal averages for the 1960s (red), 1970s (orange), 1980s (yellow), 1990s (green) and 2000s (blue). Dashed colored lines represent ECCO2's decadal averages for 1990s (magenta) and 2000s (black).

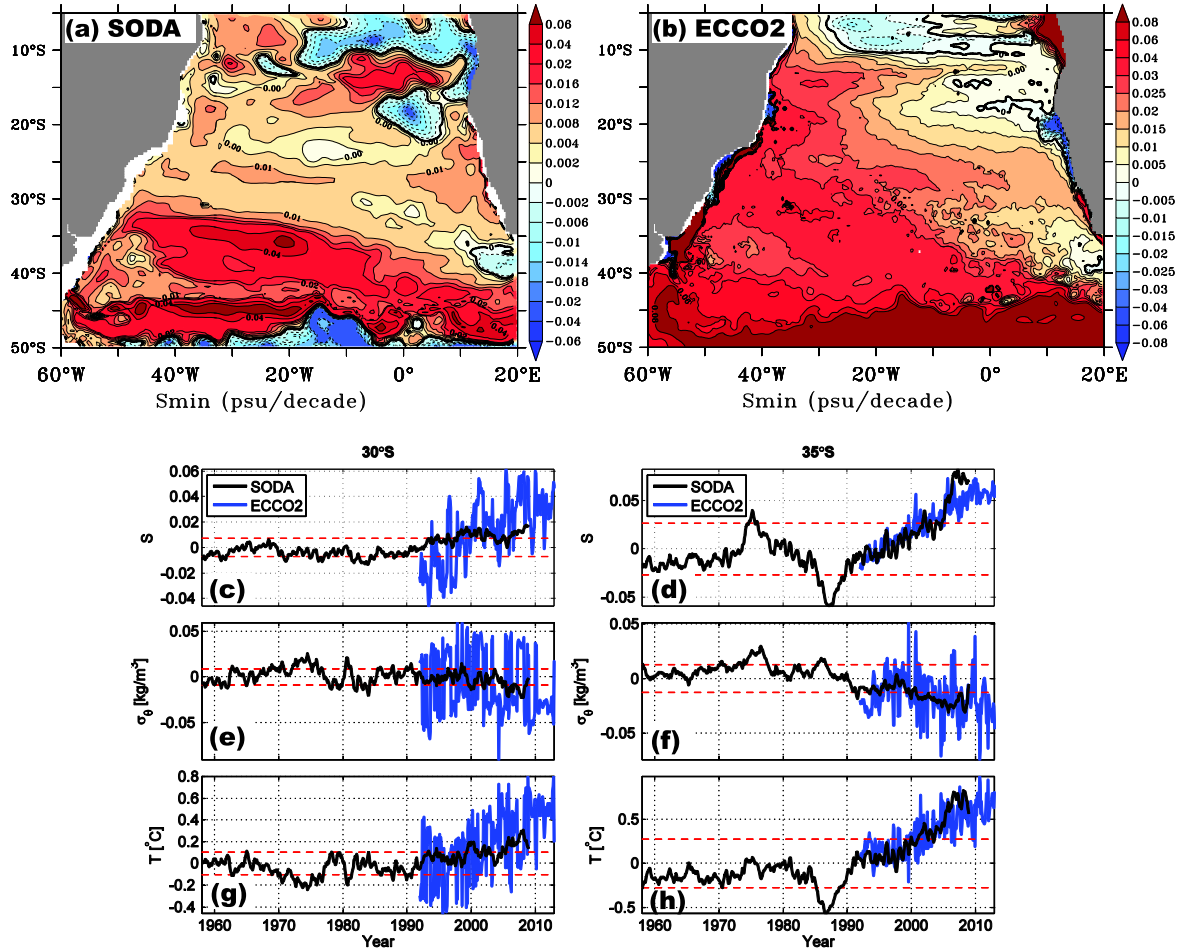


Figure 4. Salinity minimum trend between 1990's and 2000's (psu/decade) for (a) SODA and (b) ECCO2. Panels (c-h) are the time series of the salinity (c, d), sigma density (e,f), and temperature (g,h) anomalies with respect to SODA's 1960-2008 period at the location of the salinity minimum. Timeseries on the left column are for 25°W/30°S and on the right column for 25°W/35°S. Black timeseries is for SODA and blue is for ECCO2. The red dashed lines represent SODA's the three standard deviation levels relative to each parameter.

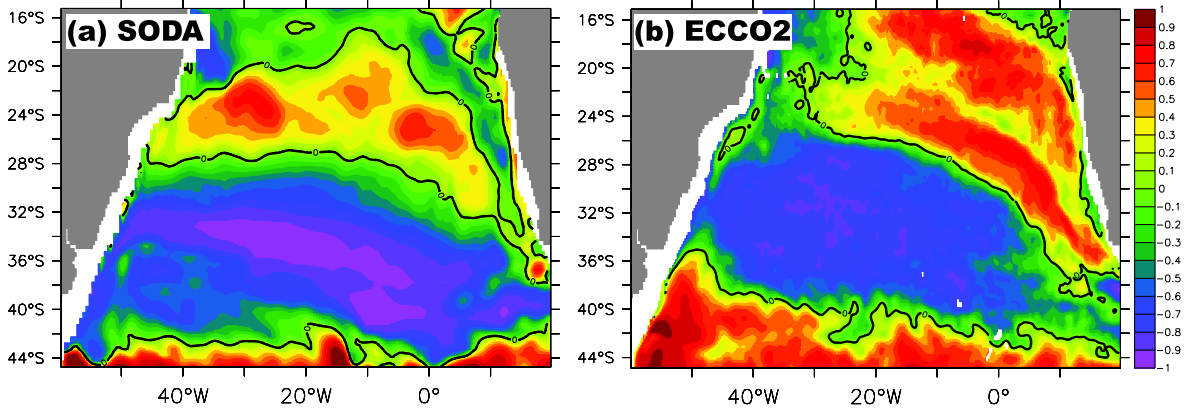


Figure 5. Correlation between the components of the sigma density, i.e., thermopycnal and halopycnal components, at approximately 1100 m depth for (a) SODA and (b) ECCO2. The components of sigma are calculated by keeping the other component as the climatological value.

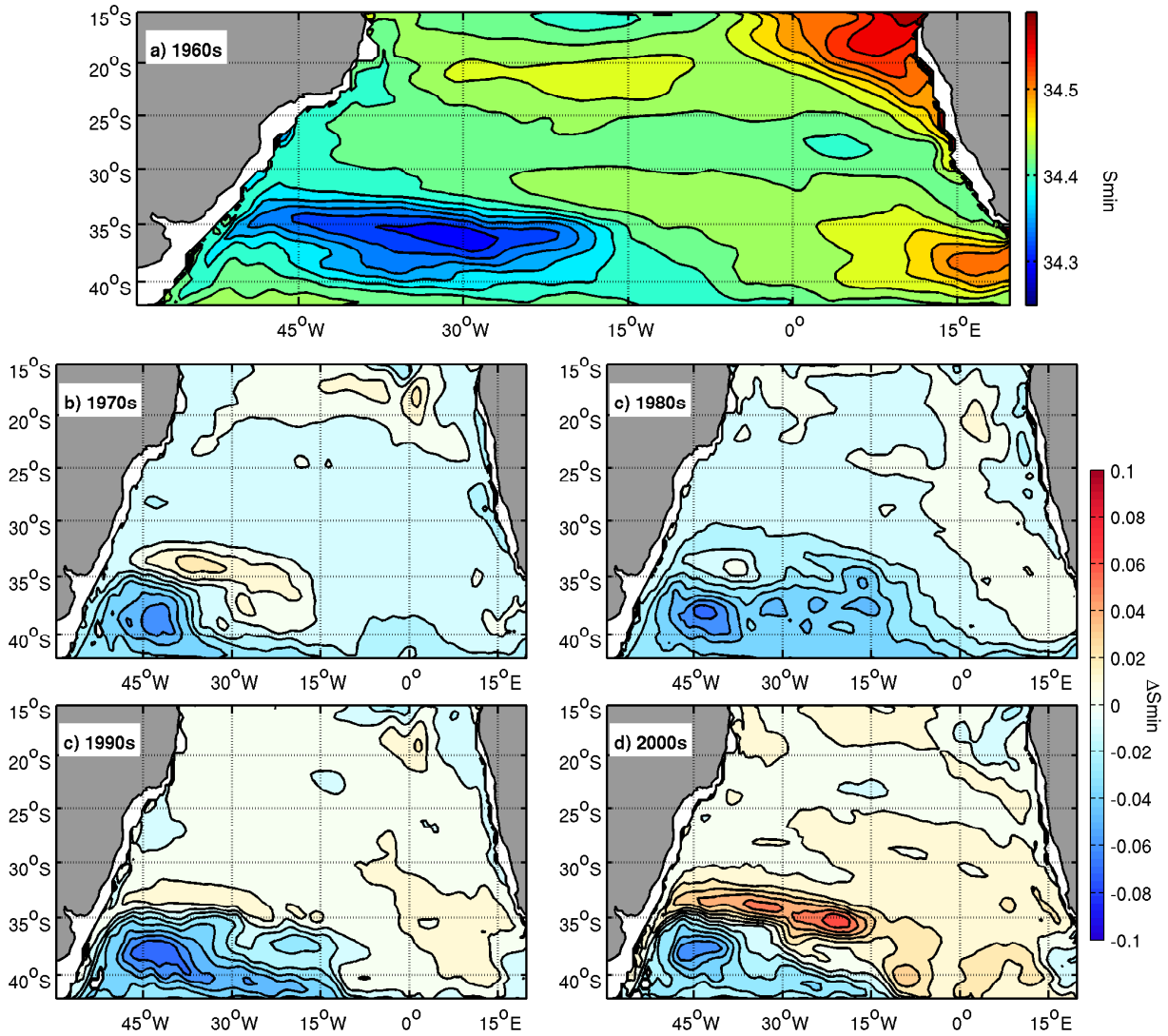


Figure 6. Salinity minimum within the layer defined by the $\gamma_n = 27.1$ and $\gamma_n = 27.6$ neutral surfaces for a) 1960s, b) 1970s, c) 1990s and d) 2000s.

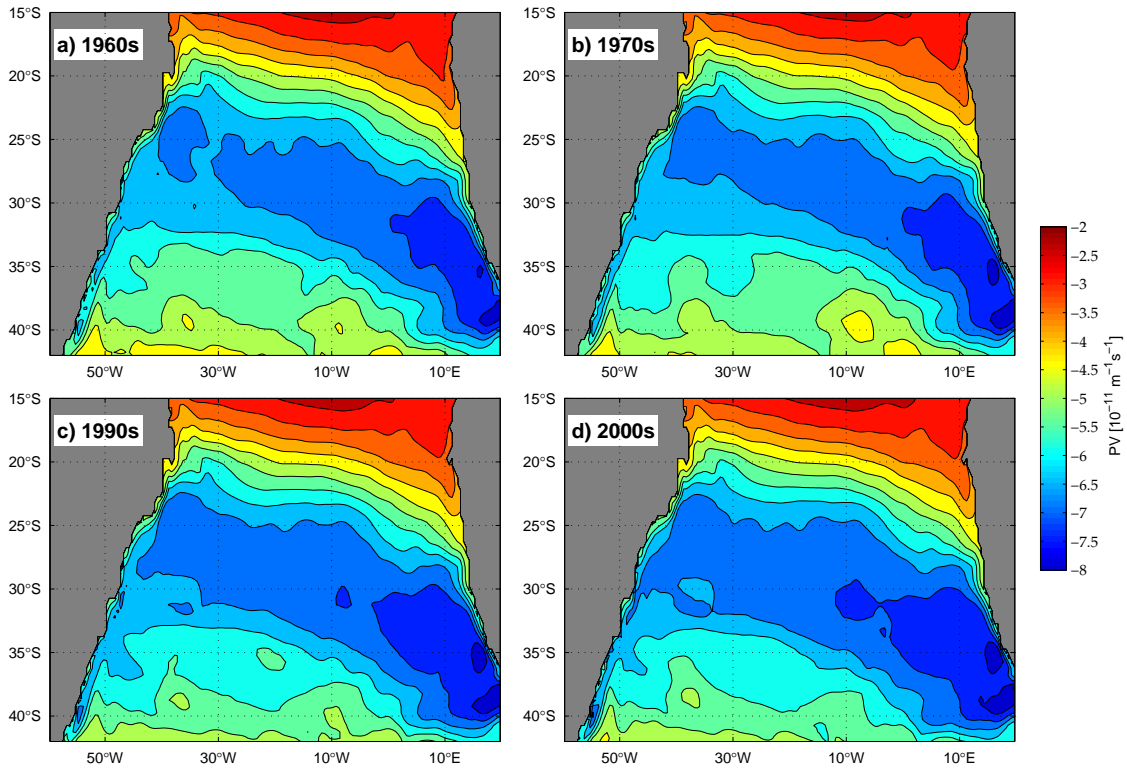


Figure 7. Ertel's potential vorticity calculated within the layer defined by the $\gamma = 27.1$ and $\gamma = 27.6$ neutral surfaces for a) 1960s, b) 1970s, c) 1990s and d) 2000s.

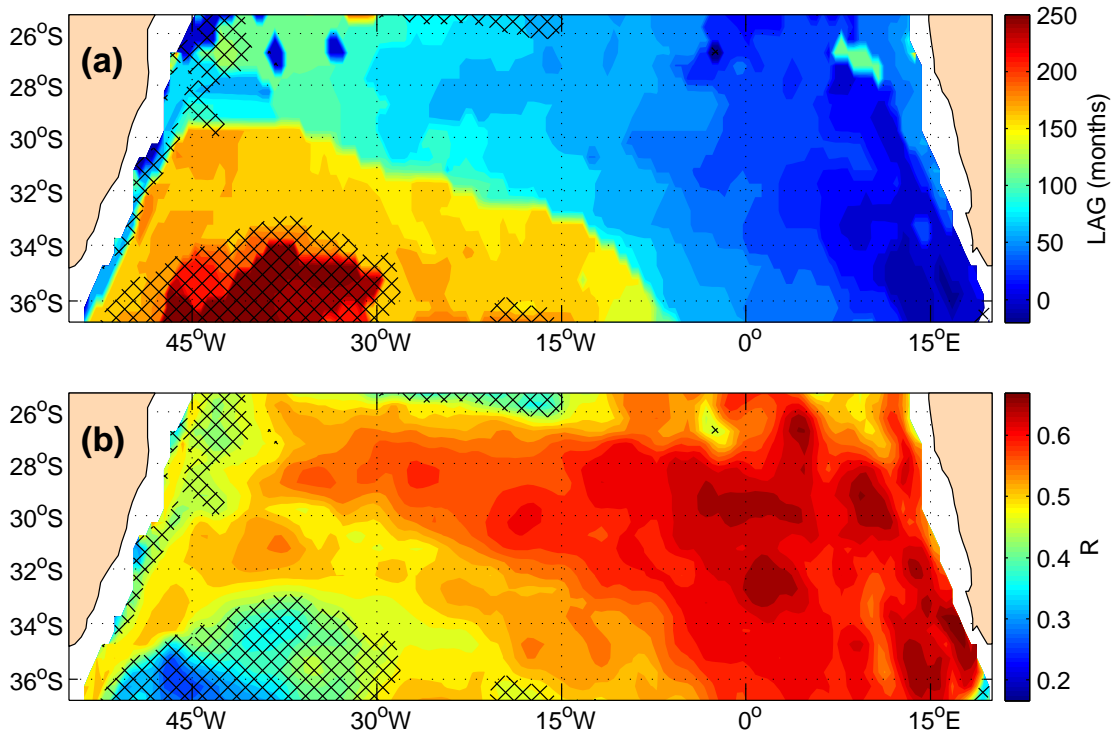


Figure 8. Maximum lagged correlation between the salinity at $\sigma_\theta = 27.2$ and a westerly wind strength index in the southeastern Atlantic, defined by the τ_x averaged between 35°S–65°S/0°E–20°E. (a) is the lag of the maximum correlation (months) and (b) is the maximum correlation. The crossed areas are where correlation values of the pre-whitened timeseries are not statistically significant.

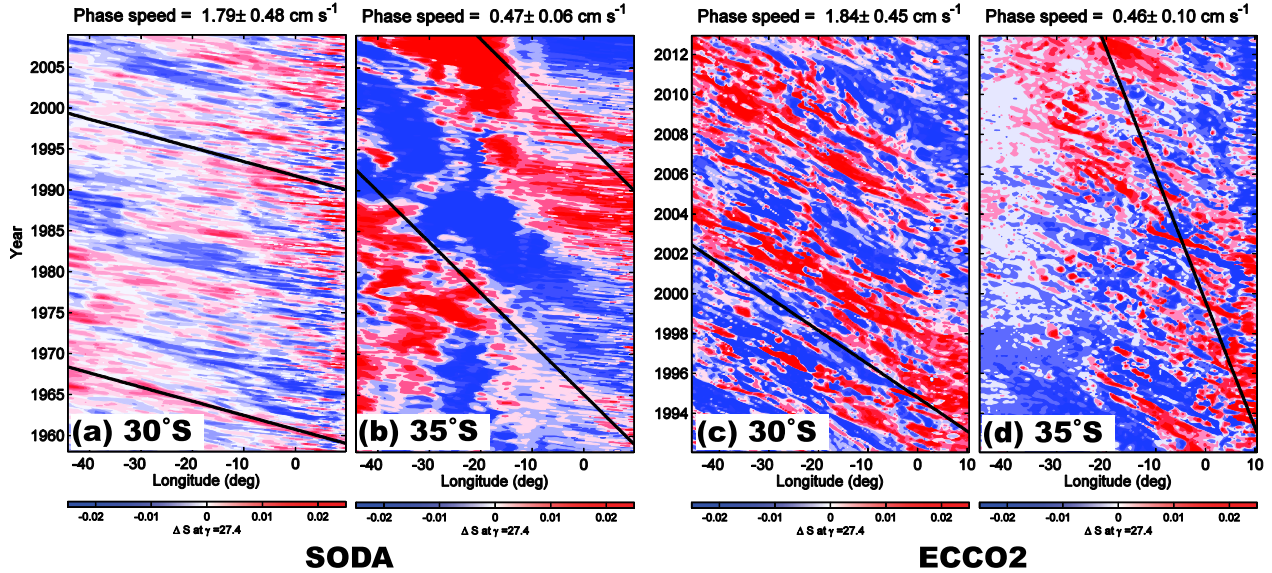


Figure 9. Time x Longitude diagram for the salinity anomalies projected onto the neutral density surface $\gamma_n = 27.4$, that defines the region of minimum salinity in the subtropical Atlantic at (a,c) 30°S and (b,d) 35°S . Panels (a,b) are for SODA and (c,d) are for ECCO2. Following *Barron et al. [2009]*, the zonal average of the salinity anomalies is subtracted from the diagrams to highlight the propagating features. The phase speed calculated from the method of *Barron et al. [2009]* is shown on the top of each panel and its displacement is shown as a black line overlaid on the contours.

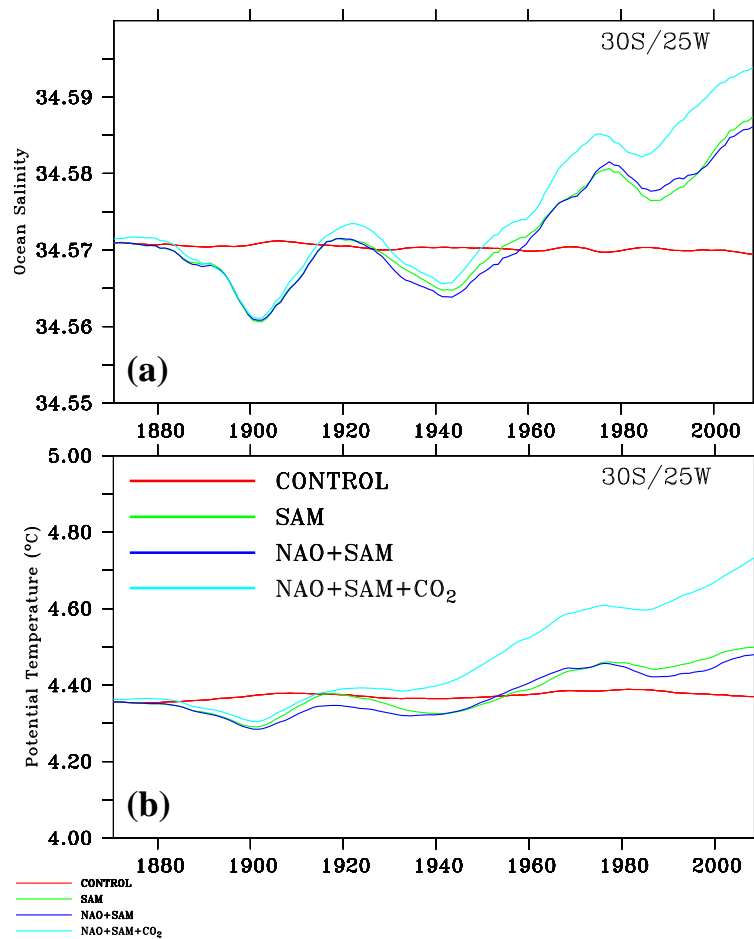


Figure 10. Time series of (a) salinity and (b) potential temperature **at the salinity minimum depth at 30°S/25°W from the UVIC model experiments.** The colored lines are for the CONTROL (red), SAM only (green), SAM plus NAO (dark blue), and NAO plus SAM plus CO₂ (cyan) experiments.

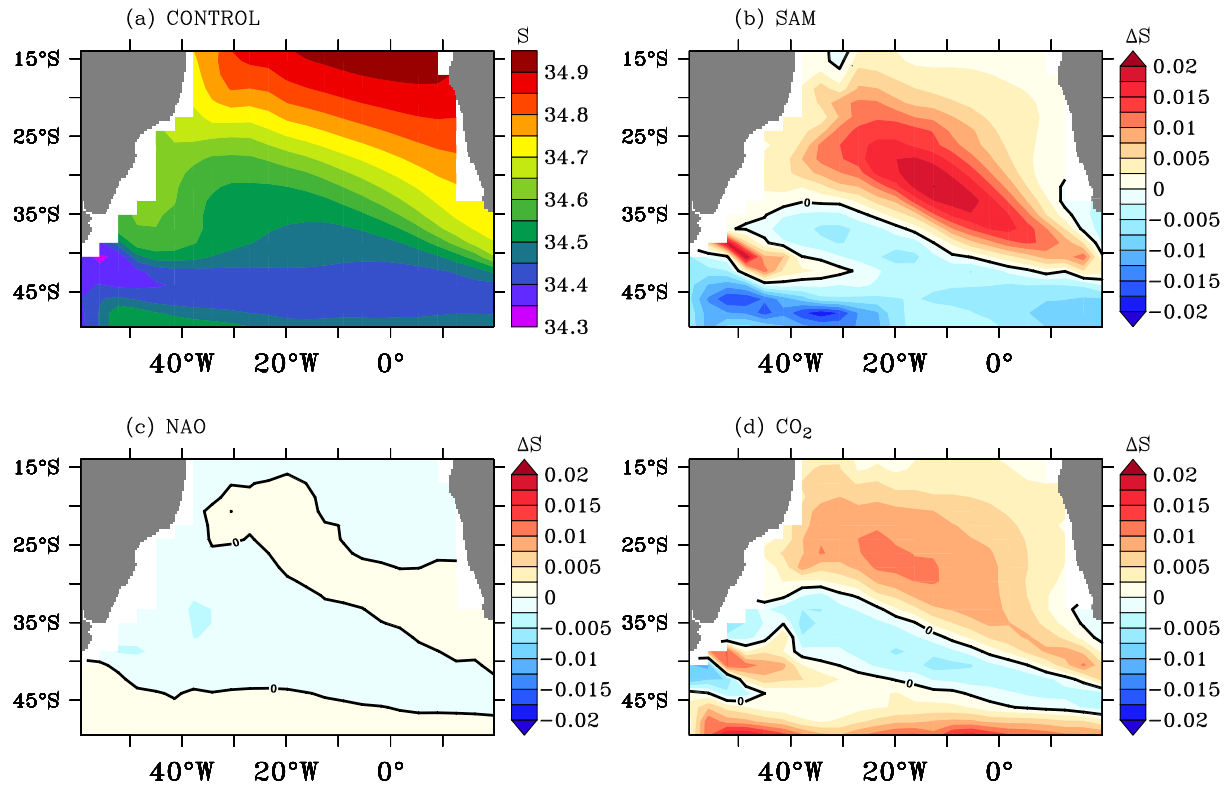


Figure 11. (a) South Atlantic salinity minimum in the Uvic CONTROL experiment averaged between 2000–2009. (b–d) Average (2000–2009) salinity minimum differences among the experiments, in which each panel shows how adding one forcing changes the salinity in comparison to the experiment without that forcing, for (b) SAM, (c) NAO, and (d) CO₂.

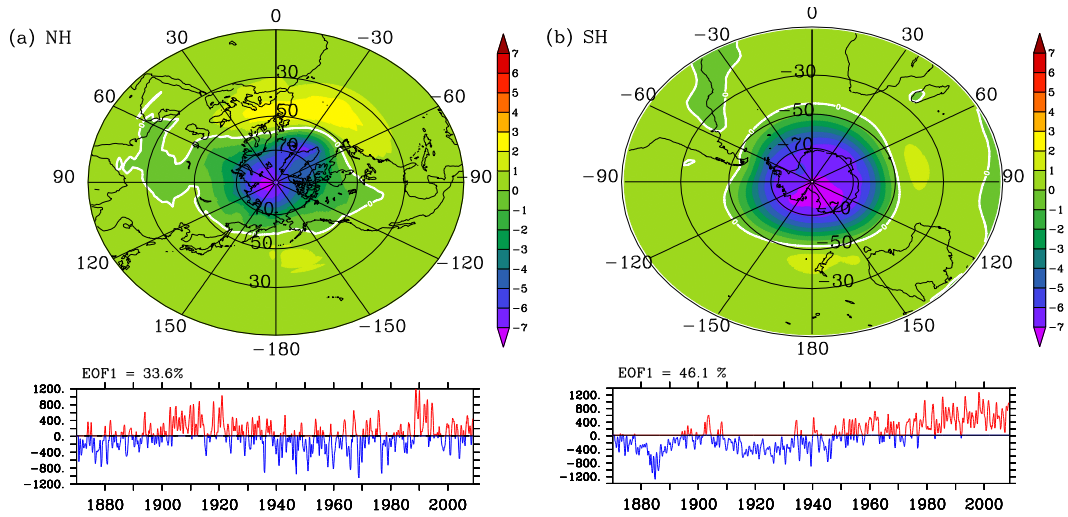


Figure 12. First EOF of the hemispheric sea level pressure used to force the atmospheric model in UVic for the (a) Northern Hemisphere and (b) Southern Hemisphere.